INTERNATIONAL JOURNAL FOR NUMERICAL METHODS IN FLUIDS
Int. J. Numer. Meth. Fluids 2003; **42**:953–977 (DOI: 10.1002/fld.564)

Development of optimized weighted-ENO schemes for multiscale compressible flows

D. Ponziani, S. Pirozzoli and F. Grasso*,†

Dipartimento di Meccanica ed Aeronautica, Università di Roma 'La Sapienza,' via Eudossiana 18, 00184 Roma, Italy

SUMMARY

The present paper deals with the development of optimized weighted–ENO schemes to improve the resolution of a class of compressible flows characterized by a wide disparity of scales, typical of compressible turbulence and/or aeroacoustic phenomena, and shock waves. The approach relies on a least square minimization of both the dispersion and dissipation error components together with the use of symmetric stencil support. Extensive numerical simulations of sound propagation, shock–sound interaction and isotropic compressible turbulence have been carried out, and the results confirm that the optimized schemes yield a resolution in wave number space greater than the non-optimized ones. Copyright © 2003 John Wiley & Sons, Ltd.

KEY WORDS: optimized high-order schemes; weighted-ENO schemes; compressible turbulence; aeroacoustics

1. INTRODUCTION

The present paper focuses on the numerical simulation of compressible flows that are generally characterized by a wide disparity of length and time scales as in the case of aeroacoustic phenomena and compressible turbulence. Hence, for an accurate resolution of all the scales, the numerical schemes must have spectral-like properties.

It is important to point out that spectral schemes are generally limited to simple geometries and (most important) are not suitable in the presence of flow discontinuities such as shock waves and/or eddy shocklets that typically occur in compressible flows. In the present work we will then consider high order conservative finite difference schemes, which are capable of accurately capturing any discontinuity. We recall that high order non-optimized schemes are normally obtained by minimizing the truncation error. For example, essentially non-oscillatory (ENO) and the most recent weighted-ENO schemes yield a uniform high order accurate interpolation if the solution is smooth, and maintain high accuracy and essentially non-oscillatory

*Correspondence to: F. Grasso, Dipartimento di Meccanica e Aeronautica, Universita di Roma, Via Eudossiana 18, 00184 Roma, Italy.
†E-mail: grasso@grasso.ing.uniroma1.it

Received 14 August 2002
Revised 7 March 2003

properties in the presence of discontinuities. However, they do not adequately resolve small scale structures (observe that for a given mesh the threshold of the best resolved scale is generally dictated by the mesh size).

In order to obtain schemes that are capable of accurately resolving a wide range of scales, the dispersion and dissipation error components have to be characterized. This can be generally achieved through a Fourier analysis of the errors associated with the approximation. Thus, by devising an error minimization procedure, (so-called) optimized schemes are obtained. Tam and Webb [1] have first addressed the problem of designing optimized finite difference schemes for the linearized Euler equations applied to computational aeroacoustics. Those authors have recognized the importance of ensuring that finite difference schemes satisfy the same dispersion relations as the original system of partial differential equations. By means of Fourier–Laplace transforms those authors have then constructed the so-called dispersion-relation-preserving (DRP) schemes by optimizing the finite difference approximation in the wave number and frequency space. In particular, they have only considered central difference schemes that have symmetric stencil support (hence, zero dissipation); as a consequence, their analysis only deals with the minimization of the dispersion error.

As pointed out by Lockard *et al.* [2] the restriction to central difference approximations to get minimal dissipation error may lead to instability that needs to be cured by an explicit addition of dissipation. Those authors have developed an optimization procedure for the solution of the Euler equations by means of essentially non-oscillatory (ENO) schemes. The optimization consists in evaluating the interpolation coefficients of all candidate stencils by minimizing the linear combination of the dispersion and dissipation errors with the additional constraint of seven points per wavelength resolution (PPW). Lockard *et al.* have applied the optimization procedure to the solution of the Euler equations and have shown that the optimized ENO schemes outperform the non-optimized ones for the case of linear wave propagation problems; however, they have concluded that their strategy is not effective for non-linear problems.

Weirs and Candler [3] have extended the work of Tam and Webb [1] to develop optimized weighted-ENO schemes for the solution of the hyperbolic conservation laws in one space dimension. In particular, those authors have devised a strategy that consists in optimizing only the weights of the linear combination of all candidate stencils by minimizing the solution error (defined in terms of a linear combination of the dissipation and phase errors). On each stencil the reconstruction is obtained through a non-optimized polynomial interpolation; in addition, in order to reduce the numerical dissipation they have also employed an additional stencil so as to consider a symmetric stencil support.

Wang and Chen [4] have developed optimized weighted-ENO schemes for the solution of the linearized Euler equations applied to shock/broadband noise interaction. Those authors have designed a two-level optimization procedure that relies on the minimization of the linear combination of the dispersion and dissipation errors. First, on each stencil the interpolation coefficients are optimized by minimizing the error (of the reconstruction on each stencil) with the constraint of resolving the short waves with six points per wavelength. Then, the linear weights are optimized as proposed by Weirs and Candler; however, they only consider unsymmetrical stencil support.

In the present paper we have devised a two-level optimization strategy for weighted-ENO schemes whereby we optimize both the interpolation coefficients of all candidate stencils and the linear weights. In addition, in order to minimize the error amplitude we have also

considered an additional stencil support as proposed by Weirs and Candler. The procedure has been applied to solve the Euler equations for the simulation of sound propagation and shock–sound interaction. Furthermore, the approach has been applied to the direct numerical simulation of isotropic compressible turbulence by solving the Navier–Stokes equations. In the following sections the numerical methodology is discussed and the optimization strategy is analysed in detail, and the results are discussed.

2. NUMERICAL METHODOLOGY

As discussed in the introduction, the equations that we solve are either the Euler or the Navier–Stokes ones. However, since the optimization procedure has been applied to construct the numerical inviscid flux, we only discuss the Euler equations that are written in the following finite difference conservative form:

$$\frac{\mathrm{d}\boldsymbol{w}_{i,j,k}}{\mathrm{d}t} + \frac{1}{\Delta x}(\hat{\boldsymbol{f}}^{(x)}_{i+1/2,j,k} - \hat{\boldsymbol{f}}^{(x)}_{i-1/2,j,k}) + \frac{1}{\Delta y}(\hat{\boldsymbol{f}}^{(y)}_{i,j+1/2,k} - \hat{\boldsymbol{f}}^{(y)}_{i,j-1/2,k}) + \frac{1}{\Delta z}(\hat{\boldsymbol{f}}^{(z)}_{i,j,k+1/2} - \hat{\boldsymbol{f}}^{(z)}_{i,j,k-1/2}) = 0 \tag{1}$$

where $\boldsymbol{w}$ and $\boldsymbol{f}$ are, respectively, the vector unknown and the inviscid flux

$$\boldsymbol{w} = [\rho, \rho u, \rho v, \rho w, \rho E]^{\mathrm{T}}$$
$$\boldsymbol{f} = [\rho \boldsymbol{u}, \rho \boldsymbol{u}\boldsymbol{u} + p\boldsymbol{I}, \rho \boldsymbol{u} H]^{\mathrm{T}},$$

and $p = \rho RT$, $H = E + p/\rho$.

Note that superscript x, y and z in Equation (1) indicate the flux component along the x, y and z directions, while subscripts i, j and k identify the grid nodes along the three directions; similarly, $\Delta x, \Delta y$ and Δz stand for the mesh spacings (in the three directions). Observe that the present scheme has been developed by using cartesian co-ordinates; however, it can easily be extended to more general curvilinear coordinates provided one introduces a strong conservation form of the equations [5].

In order to ensure conservation and high resolution of the discretized equations, we have employed a finite difference approximation that is based on the use of weighted-ENO (WENO) schemes [6–8]. The basic idea of WENO is to introduce a convex linear combination of low-order polynomial reconstructions that yield a high order accuracy in smooth regions.

For simplicity, let us refer to the one-dimensional scalar problem $v_{\mathrm{t}} + f(v)_x = 0$.

Given the pointwise values of the function $v(x,t)$ and assuming a uniform grid, the problem is to find a numerical flux function $\hat{f}_{i+1/2}$, such that the following condition is satisfied

$$\left.\frac{\partial f}{\partial x}\right|_{x=x_i} = \frac{1}{\Delta x}(\hat{f}_{i+1/2} - \hat{f}_{i-1/2}) + \mathcal{O}(\Delta x^{2s-1}) \tag{2}$$

where $2s-1$ is the formal order of accuracy. In the present work we have used a flux splitting approach and the numerical flux function is determined as

$$\hat{f}_{i+1/2} = \hat{f}^{+}_{i+1/2} + \hat{f}^{-}_{i+1/2} \tag{3}$$

where $\hat{f}^+$ and $\hat{f}^-$ are the positive and negative parts of the flux that are associated, respectively, to the negative and positive flux jacobian. Hence, $\hat{f}^{\pm}_{i+1/2}$ are reconstructed from the pointwise values $f^{\pm}_j$, i.e.

$$\hat{f}^{\pm}_{i+1/2} = \mathbf{R}\,(\, f^{\pm}_j;\ j = i-s+1, i+s)$$

where $\mathbf{R}$ indicates the reconstruction operator; the values of $f^{\pm}_j$ are defined, for example, in terms of the local Lax–Friedrichs scheme according to

$$f^{\pm}_j = \frac{1}{2}(\, f(v) \pm \gamma v)_j \tag{4}$$

where

$$\gamma = \max_{i-s+1,\ldots,i+s} |\partial f/\partial v|$$

In the following we briefly revise the WENO approach. The reconstruction operator relies on a convex linear combination of s polynomial interpolations (q) of order $s-1$. For example, the numerical flux function $\hat{f}^+_{i+1/2}$ is obtained according to

$$\hat{f}^+_{i+1/2} = \sum_{r=0}^{s-1} \omega^+_r\, q^+_r(x_{i+1/2}) = \sum_{r=0}^{s-1} \omega^+_r \sum_{l=0}^{s-1} c^+_{r,l}\, f^+_{i-r+l} \tag{5}$$

where ω^+_r are the non-linear weights and $c^+_{r,l}$ are the interpolation coefficients over the rth s-point stencil $S^+_r = \{x_{i-r}, \ldots, x_{i-r+s-1}\}$, with $r = 0, \ldots, s-1$; similarly, $\hat{f}^-_{i+1/2}$ is obtained through a polynomial reconstruction over the s-point stencils with $S^-_r = \{x_{i-r}, \ldots, x_{i-r+s-1}\}$, and $r = -1, \ldots, s-2$.

In order to ensure a convex combination of all candidate stencils the non-linear weights (ω^+) have to satisfy the requirements

$$\omega^+_r \geqslant 0, \quad \sum_{r=0}^{s-1} \omega^+_r = 1 \tag{6}$$

In particular, as originally proposed by Shu [7] we set

$$\omega^+_r = \frac{d^+_r/(\varepsilon + \beta^+_r)^2}{\sum_{m=0}^{s-1} d^+_m/(\varepsilon + \beta^+_m)^2} \tag{7}$$

where d^+_r, β^+_r and ε are, respectively, the linear weights, the smoothness indicators and a small parameter (introduced to avoid division by zero) [5, 9]. The coefficients β^+_r are a measure of the smoothness of the rth polynomial reconstruction $q^+_r(x)$ over the interval $[x_{i-1/2}, x_{i+1/2}]$. Wang and Chen [4] have shown that the accuracy of a WENO scheme is strongly dependent upon the definition of β^+_r, which is critical in order to distinguish short waves from discontinuities. In the present work we have used the original definition of Shu [7]; we have also tested the definition proposed by Wang and Chen [4], however the results obtained (not reported) do not yield any significant improvement for the test cases that we have selected.

The previous method has been extended to determine the numerical inviscid flux function of the system of conservation laws corresponding to Equation (1) by considering a local

characteristic flux decomposition in each coordinate direction, see [8]. For example, referring to the x-direction, the procedure involves the following steps:

- The average state at $(i+1/2, j, k)$ is determined in terms of Roe's average.
- The left ($\boldsymbol{L}^{(x)}$) and right ($\boldsymbol{R}^{(x)}$) eigenvector matrices (and similarly the eigenvalues $\boldsymbol{\Lambda}^{(x)}$) of the Jacobian matrix ($\partial \boldsymbol{f}^{(x)}/\partial \boldsymbol{w}$) are evaluated at the average state (indicated by *).
- For each stencil, the conservative variables and the fluxes are projected onto the local characteristic eigendirections

$$\mathbf{w}_{\ell,j,k} = \boldsymbol{L}^{(x)^*} \boldsymbol{w}_{\ell,j,k}, \quad \ell \in [i-s+1, i+s] \tag{8}$$

$$\mathbf{f}_{\ell,j,k} = \boldsymbol{L}^{(x)^*} \boldsymbol{f}_{\ell,j,k}, \quad \ell \in [i-s+1, i+s] \tag{9}$$

- The pointwise characteristic fluxes are determined according to

$$\mathbf{f}^{\pm}_{\ell,j,k} = \frac{1}{2}(\mathbf{f}_{\ell,j,k} \pm \gamma \mathbf{w}_{\ell,j,k}), \quad \ell \in [i-s+1, i+s] \tag{10}$$

  where

$$\gamma = \max_{\ell = i-s+1, i+s} |\Lambda^{(x)^*}_{\ell,j,k}|$$

  that corresponds to the use of the local Lax–Friedrichs scheme.
- The numerical characteristic flux functions $\hat{\mathbf{f}}^{\pm}_{i+1/2,j,k}$ are reconstructed from the pointwise values $\mathbf{f}_{\ell,j,k}$.
- The numerical flux function is finally computed according to

$$\boldsymbol{f}^{(x)}_{i+1/2,j,k} = \boldsymbol{R}^{(x)^*}(\hat{\mathbf{f}}^{+}_{i+1/2,j,k} + \hat{\mathbf{f}}^{-}_{i+1/2,j,k})$$

The contributions of the fluxes in the y- and z-directions are obtained similarly.

2.1. Optimization of WENO schemes

In this section we describe the procedure to design optimized WENO schemes. Let s be the number of stencils (each one having a s-point support); we first recall that, according to their original formulation (reported for example in References [7, 8]), the non-optimized interpolation coefficients are determined through a Taylor series expansion to obtain an accuracy of order p_1 on each stencil. For example, the coefficients $c^{+}_{r,l}$ of the rth stencil are obtained from

$$\sum_{l=0}^{s-1} c^{+}_{r,l}[(-r+l)^{j+1} - (-r+l-1)^{j+1}] = \delta_{j0}, \qquad \begin{matrix} j = 0, \ldots, p_1 - 1 \\ r = 0, \ldots, s-1 \end{matrix} \tag{11}$$

where δ is the Kronocker delta.

For the non-optimized WENO schemes

$$p_1 = s$$

Similarly, the linear weights (d_r^+) are determined through a Taylor series expansion over all stencils according to

$$\sum_{r=0}^{s-1} d_r^+ \sum_{l=0}^{s-1} c_{r,l}^+ [(-r+l)^{j+1} - (-r+l-1)^{j+1}] = \delta_{j0}, \quad j = 0, \ldots, p_1 + p_2 - 1 \tag{12}$$

Non-optimized WENO schemes satisfy the relation

$$p_2 = s - 1$$

and have a formal order of accuracy $p_1 + p_2 = 2s - 1$, provided the f^+ are smooth over the s candidate stencils.

The weights d_r^- are determined through a similar procedure while the interpolation coefficients $c_{r,l}^-$ satisfy the following relation

$$c_{r-1,l}^- = c_{s-r-1,s-1-l}^+, \quad r, l = 0, \ldots, s-1$$

It is important to recall that WENO schemes have generally been designed to achieve high order accuracy without paying too much attention to their spectral resolution properties. Conversely, optimized WENO schemes extend the range of well resolved wave numbers at the expense of formal accuracy. Indeed, the primary goal of the optimization is to minimize the dispersion error so as to achieve a spectral-like resolution and to have a numerical dissipation capable of damping the oscillations in the presence of discontinuities.

In order to design optimized difference schemes, the formal order of approximation is reduced so as to provide additional degrees of freedom that are then exploited to optimize the spatial discretization operator. In principle, one can optimize the interpolation coefficients and/or the linear weights; in the present paper we have devised a multilevel optimization strategy (referred to as OPPG-WENO) that uses a symmetric stencil support in order to ensure that the dissipation is minimal. This is achieved by including an additional candidate stencil that corresponds to extending the summation in r in Equation (5) to s (rather than $s-1$) and Equations (11) and (12) become

$$\sum_{l=0}^{s-1} c_{r,l}^+ [(-r+l)^{j+1} - (-r+l-1)^{j+1}] = \delta_{j0}, \qquad \begin{matrix} j = 0, \ldots, p_1 - 1 \\ r = 0, \ldots, s \end{matrix} \tag{13}$$

$$\sum_{r=0}^{s} d_r^+ \sum_{l=0}^{s-1} c_{r,l}^+ [(-r+l)^{j+1} - (-r+l-1)^{j+1}] = \delta_{j0}, \quad j = 0, \ldots, p_1 + p_2 - 1 \tag{14}$$

Referring to the scalar advection problem $\partial v/\partial t + \partial v/\partial x = 0$, the modified wave number [29] for each stencil ($\tilde{\alpha}_r$) is

$$\tilde{\alpha}_r = 2\, \mathrm{e}^{-i\alpha/2}\, \sin(\alpha/2) \sum_{l=0}^{s-1} c_{r,l}^+ \mathrm{e}^{i\alpha(-r+l)} \tag{15}$$

The interpolation coefficients are then determined as follows

- For each stencil, $p_1 < s$ conditions are prescribed by enforcing the satisfaction of the Taylor series expansion according to Equation (13).

- The remaining $s - p_1$ conditions are determined by minimizing the error E_r (on the rth stencil) in wave number space

$$\frac{\partial E_r}{\partial c^+_{r,l}} = 0, \quad l = p_1, \ldots, s-1, \quad r = 0, \ldots, s \tag{16}$$

where E_r is defined as

$$E_r = \int_0^{\alpha_{\max}} g_c(\alpha) \{[\mathrm{Re}(\tilde{\alpha}_r) - \alpha]^2 + [\mathrm{Im}(\tilde{\alpha}_r) + f_c(\alpha)]^2\} \, \mathrm{d}\alpha \tag{17}$$

where $\alpha_{\max}$ identifies the range of wave numbers where optimization is effective; g_c is a weight function that is introduced in order to emphasize the error in the wave number range where the spectrum is better resolved, and the function f_c is introduced to ensure the generation of a minimal dissipation [2].

The linear weights are optimized according to the following procedure

- $p_2 + 1$, with $p_2 < s$, conditions corresponding to Equation (14) are imposed.
- The remaining $s - p_2$ relations are determined by minimizing the solution error (E) over all stencils

$$E = \int_0^{\alpha_{\max}} g_d(\alpha) \{[\mathrm{Re}(\tilde{\alpha}) - \alpha]^2 + [\mathrm{Im}(\tilde{\alpha}) + f_d(\alpha)]^2\} \, \mathrm{d}\alpha \tag{18}$$

where

$$\tilde{\alpha} = \sum_{r=0}^{s} d_r^+ \tilde{\alpha}_r$$

is the modified wave number of the overall scheme, and g_d and f_d play the same role as g_c and f_c.

The following relations are then imposed

$$\frac{\partial E}{\partial d_r^+} = 0, \quad r = p_2 + 1, \ldots, s$$

As originally proposed by Weirs and Candler [3], the smoothness indicator associated to the additional stencil is evaluated as the maximum over all stencils (i.e. $\beta_s = \max_{r=0,s} \beta_r$) so as to prevent the selection of fully downwinded stencils.

With regard to the functions f and g, we have considered the following functional forms

$$g(\alpha) = 1 \quad \text{or} \quad g(\alpha) = \mathrm{e}^{v(\pi - \alpha)} \tag{19}$$

$$f(\alpha) = 0 \quad \text{or} \quad g(\alpha) = \sin^{\mu} \alpha/2, \tag{20}$$

whose combination leads to different optimization procedures, including the ones proposed by Wang and Chen [4] and Weirs and Candler [3].

For a given s, the optimal strategy depends upon the parameters p_1, p_2, v, $\alpha_{\max}$ and μ; we have then carried out an extensive analysis (whose details are not reported) in order to determine the optimal values of the parameters. By analysing the dispersion and the dissipation properties associated to the various schemes, the analysis furnishes $p_1 = 1$, $p_2 = 0$, $v = 6$, and

Table I. Interpolation coefficients ($c^+_{r,l}$) and linear weights (d_r) for $s=3$.

	c^+_{rj}	$j=0$	$j=1$	$j=2$	d^+_r
WENO$_5$	$r=0$	1/3	5/6	−1/6	3/10
	$r=1$	−1/6	5/6	1/3	3/5
	$r=2$	1/3	−7/6	11/6	1/10
OWENO$_{51}$	$r=0$	0.38043	0.81691	−0.19734	0.34263
	$r=1$	−0.19734	0.81691	0.38043	0.53608
	$r=2$	0.37231	−1.02576	1.65345	0.12129
OPPG-WENO$_5$	$r=-1$	1.65345	−1.02576	0.37231	0.08613
	$r=0$	0.38043	0.81691	−0.19734	0.38179
	$r=1$	−0.19734	0.81691	0.38043	0.42235
	$r=2$	0.37231	−1.02576	1.65345	0.10973

Table II. Interpolation coefficients ($c^+_{r,l}$) and linear weights (d_r) for $s=4$.

	c^+_{rj}	$j=0$	$j=1$	$j=2$	$j=3$	d^+_r
WENO$_7$	$r=0$	1/4	13/12	−5/12	1/12	4/35
	$r=1$	−1/12	7/12	7/12	−1/12	18/35
	$r=2$	1/12	−5/12	13/12	1/4	12/35
	$r=3$	−1/4	13/12	−23/12	25/12	1/35
OWENO$_{73}$	$r=0$	0.28419	1.03182	−0.41620	0.10019	0.14150
	$r=1$	−0.10077	0.60077	0.60077	−0.10077	0.48617
	$r=2$	0.10019	−0.41620	1.03182	0.28419	0.33383
	$r=3$	−0.27941	0.98166	−1.62508	1.92283	0.03850
OPPG-WENO$_7$	$r=-1$	1.88394	−1.54166	0.89824	−0.24052	0.03810
	$r=0$	0.28951	1.02041	−0.40479	0.09487	0.09952
	$r=1$	−0.10077	0.60077	0.60077	−0.10077	0.48196
	$r=2$	0.09487	−0.40479	1.02041	0.28951	0.30085
	$r=3$	−0.24052	0.89824	−1.54166	1.88394	0.07957

$\mu=16$; the study also indicates that the optimal definitions for determining the c's and the d's are

$$E_r = \int_0^{\alpha_{\max}} \{[\mathrm{Re}(\tilde{\alpha}_r) - \alpha]^2 + [\mathrm{Im}(\tilde{\alpha}_r)]^2\}\, \mathrm{d}\alpha \tag{21}$$

with $\alpha_{\max} = 0.35\pi$ (which corresponds to approximately a six points-per-wavelength resolution (PPW $= 2\pi/\alpha$); note that the same value has been used by Wang and Chen [4]);

$$E = \int_0^{\pi} \mathrm{e}^{\nu(\pi-\alpha)} \{[\mathrm{Re}(\tilde{\alpha}) - \alpha]^2 + [\mathrm{Im}(\tilde{\alpha}) + \sin^{\mu}\alpha/2]^2\}\, \mathrm{d}\alpha \tag{22}$$

which is the same error definition originally proposed by Lockard *et al.* [2] and also used by Weirs and Candler [3]. The values of the coefficients $c^+_{r,l}$ and d^+_r thus obtained are listed in Tables I and II for $s=3$ and 4, respectively.

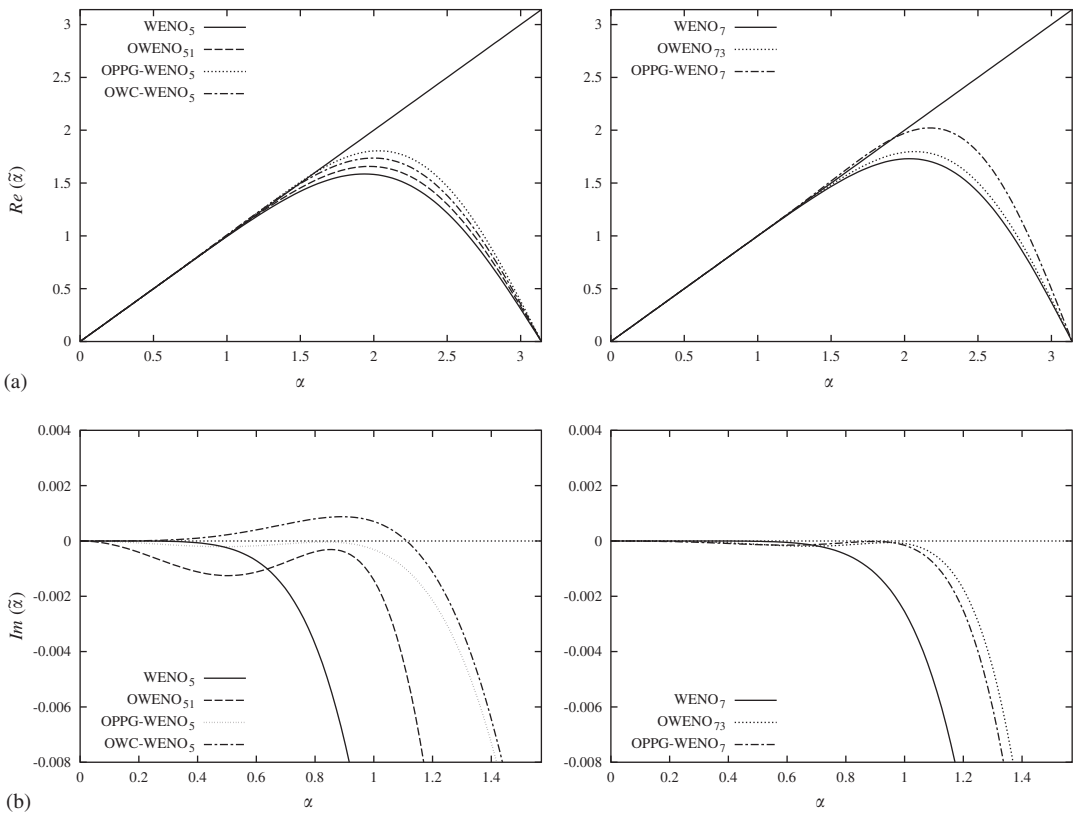

Figure 1. Linear wave propagation: distribution of the modified wave number ($\tilde{\alpha}$). (a), Real part; (b), Imaginary part.

2.2. *Dispersive and dissipative properties of the optimized schemes*

The dispersive and dissipative properties of the optimized schemes have been analysed (with reference to the linear scalar advection problem) considering WENO schemes of various order of accuracy. The distributions of the real and of the imaginary part of the modified wave number $\tilde{\alpha}$ are depicted in Figure 1 as a function of the wave number α. In the figure we also report the results corresponding to the optimization strategy of Wang and Chen [4] (referred to as OWENO) and the one proposed by Weirs and Candler [3] (referred to as OWC-WENO). The former corresponds to using an unsymmetrical stencil support and $g=1$, $f=0$. The latter uses: i) a symmetric stencil support with $p_1=s$ (i.e. the c's are not optimized); and ii) $g_{\mathrm{d}}=\mathrm{e}^{\nu(\pi-\alpha)}$, $f_{\mathrm{d}}=\sin^{\mu}\alpha/2$.

For clarity, the results are identified with subscripts that stand for the formal order of accuracy of the corresponding non-optimized and optimized WENO schemes; for example, OWENO_{51} indicates that the order of the WENO scheme is 5 while the order of the optimized scheme is 1 (i.e. $p_1+p_2=1$). Note that OWC-WENO has an accuracy of order s, while OPPG-WENO is formally first order accurate and the second subscript is omitted for both.

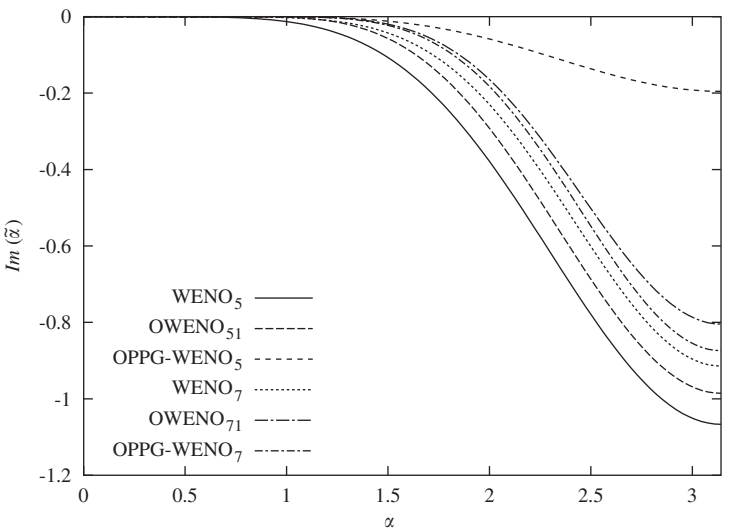

Figure 2. Linear wave propagation: distribution of the imaginary part of the modified wave number.

Figure 1 shows that all three optimization strategies increase the range of well-resolved wave numbers; however, OPPG-WENO exhibits a better wave number resolution. With regard to the optimization of the 7th order WENO schemes, we only report those that have the best wave number resolution.

The distribution of the imaginary part of the modified wave number as a function of α is reported in Figures 1 and 2, which show that OPPG-WENO$_5$ is less dissipative than all the other schemes. The figures also confirm that the schemes that have an unsymmetrical stencil support are more dissipative. Observe that for OPPG-WENO$_7$ we have set $\mu = 10$ rather than $\mu = 16$ in order to ensure the selection of stable stencils. The figures also show that the imaginary part of the modified wave number associated to OWC-WENO is positive up to a value of α that depends upon the point-per-wavelength resolution. In particular, OWC-WENO$_5$ does not prevent the dissipation error from becoming positive, thus leading to the selection of weakly unstable stencils if PPW > 6. Note that this behavior has not been pointed out by Weirs and Candler, see Figure 9 of Reference [3]. However, such a deficiency may not be observed on short times. In any case in the following we will only compare OWENO and OPPG-WENO.

3. RESULTS

In order to analyse the behavior of OPPG-WENO and the effect of the increase in the range of well resolved wave numbers, various test problems have been computed amounting to a single and broadband sound wave propagation, shock–sound interaction and isotropic compressible turbulence. The properties of OPPG-WENO have been analysed and compared with OWENO; in addition, for reference, we have also carried out computations with the non-

Table III. Sound wave propagation: norms of error (e_N) for $\lambda = 1/4$, $N = 256$, PPW $= 64$.

	L_∞	L_2	L_1
$WENO_5$	0.96100 E-09	0.67324 E-09	0.60507 E-09
$OWENO_{51}$	0.68815 E-05	0.48591 E-05	0.43685 E-05
OPPG-$WENO_5$	0.19582 E-07	0.13816 E-07	0.12451 E-07
$WENO_7$	0.20002 E-11	0.14388 E-11	0.11985 E-11
$OWENO_{73}$	0.22958 E-07	0.16185 E-07	0.14553 E-07
OPPG-$WENO_7$	0.80802 E-06	0.57056 E-06	0.51382 E-06

optimized WENO schemes. Note that the discretized governing equations have been integrated in time by means of the low storage fourth order accurate Runge–Kutta algorithm of Shu and Osher [6].

3.1. Single and broadband sound wave

The first test case corresponds to a sound wave that propagates in the positive x-direction assuming a uniform mean flow; at $t = 0$ we set

$$\begin{aligned} p(x,0) &= p_0(1 + \varepsilon \sin 2\pi x/\lambda) \\ \rho(x,0) &= \rho_0[p(x,0)/p_0]^{1/\gamma} \\ u(x,0) &= u_0 + \frac{2}{\gamma - 1}[c(x,0) - c_0] \\ v(x,0) &= 0 \end{aligned} \tag{23}$$

where $c = \gamma\, p/\rho$ is the speed of sound. Periodic boundary conditions are imposed at all boundaries. Several computations have been carried out for various wavelengths (λ) and total number of grid points (N) assuming $\varepsilon = 0.001$. In particular, we have considered the cases $\lambda = 1/4$ and $\lambda = 1/32$, and $N = 256$ and 1024 (corresponding to a PPW resolution that ranges between 8 and 64). For the small wavelength case ($\lambda = 1/32$) the wave has been let to propagate for 8 periods, while for the case corresponding to the large wavelengths ($\lambda = 1/4$) the simulations have been carried out up to one time period. The computations on the finest grid have been carried out assuming a unit CFL number. Let N_f and N_c indicate the number of grid nodes, respectively, on the fine and on the coarse grid; in order to minimize the effect of the time discretization error, the CFL number on the coarse grid has then been reduced by the factor $N_\mathrm{f}/N_\mathrm{c}$. Let $e_N = |p_N - p^*|$ be the error on the pressure, where p^* is the exact solution and p_N the solution on the grid whose size is N. In Tables III and IV we report the L_1, L_2 and L_∞ norms of the error only for the case $N = 256$ and for PPW $= 8$, 64. The results show that the optimization procedure is effective on grids whose point per wavelength resolution is $\leqslant O(10)$. However, in agreement with the findings on the dissipative properties of the scheme, as the grid resolution increases (i.e. the PPW increases) the optimization is less and less effective since the performance of all the schemes is controlled by the formal order of accuracy of the scheme. In Table V we also report the computational effort of the various schemes (measured in terms of the CPU time in seconds) for a given level of accuracy (in L_2 norm). The results confirm that the optimized schemes are more efficient that the standard ones.

Table IV. Sound wave propagation: norms of error (e_N) for $\lambda = 1/32$, $N = 256$, PPW = 8.

	L_∞	L_2	L_1
$WENO_5$	0.19534 E-03	0.14429 E-03	0.13258 E-03
$OWENO_{51}$	0.29710 E-04	0.20218 E-04	0.17861 E-04
OPPG-$WENO_5$	0.14430 E-05	0.10246 E-05	0.90506 E-06
$WENO_7$	0.31604 E-04	0.20388 E-04	0.18389 E-04
$OWENO_{73}$	0.14036 E-04	0.81113 E-05	0.67583 E-05
OPPG-$WENO_7$	0.37155 E-04	0.25729 E-04	0.22831 E-04

Table V. Sound wave propagation at $\lambda = 1/32$: CPU time (in seconds) and corresponding PPW resolution (in parentheses) to achieve a given level of accuracy in L_2 norm.

	$L_2 = 10^{-4}$	$L_2 = 2 \times 10^{-4}$
$WENO_5$	46.83 (8.8)	11.79 (7.4)
$OWENO_{51}$	33.62 (6.1)	7.41 (5.7)
OPPG-$WENO_5$	31.42 (6.0)	7.05 (5.5)
$WENO_7$	36.05 (6.2)	8.28 (5.5)
$OWENO_{73}$	29.45 (5.3)	6.32 (4.9)
OPPG-$WENO_7$	26.93 (5.0)	6.05 (4.7)

In order to test the procedure for an acoustic disturbance characterized by different length scales and a given power spectrum, we have considered the following broadband wave:

$$p(x,0) = 1 + \varepsilon e \sum_{k=1}^{N/2} E_p(k)^{1/2} \sin(2\pi x/\lambda + \psi_k) \tag{24}$$

where

$$E_p(k) = \left(\frac{k}{k_0}\right)^4 \mathrm{e}^{-2(k/k_0)^2} \tag{25}$$

is the power spectrum (with $k = 1/\lambda$) and $k_0 = 1/\lambda_0$ is the 'wave number per unit length' for which E_p attains its maximum; in addition, ψ_k is a randomly generated phase and ε is a small parameter (set equal to 0.001). For the present calculations we have selected the values $\lambda_0 = 1/4$, that implies that most of the energy is concentrated in the small wave number range, and $\lambda_0 = 1/16$ (implying that the small scales are the most relevant ones). The simulations have been carried out on various grids up to a time for which the wave front has travelled approximately 8 periods. In particular, for the case $k_0 = 4$ we have considered $N = 32$ and 64 (that have respectively an 'average' PPW of 7 and 14); for the case $k_0 = 16$ we have considered three grids $N = 64, 128$ and 256 (that have an average PPW of 4, 7 and 14). In Figures 5–9 we report the computed spectra both for the optimized and non-optimized schemes as a function of the wave number, while Figures 3–4 depict the spatial distributions of the pressure. The figures show that OPPG-WENO increases the threshold value of the well resolved scales and it outperforms OWENO. Similarly, the figures again show that the optimization is less and less effective as the number of points per wavelength increases. In

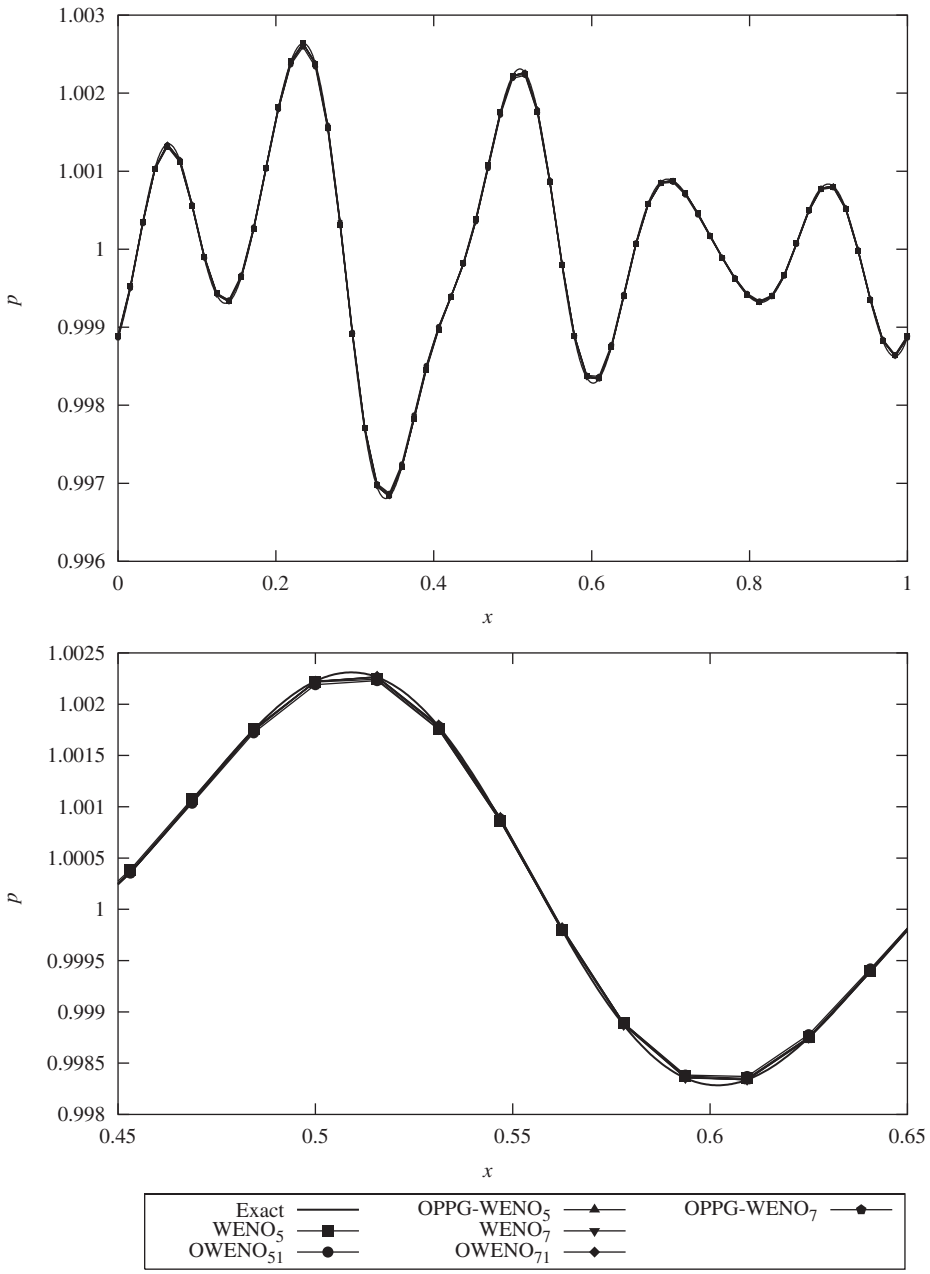

Figure 3. Broadband wave propagation. Distribution of the acoustic pressure ($k_0 = 4,\ N = 64$).

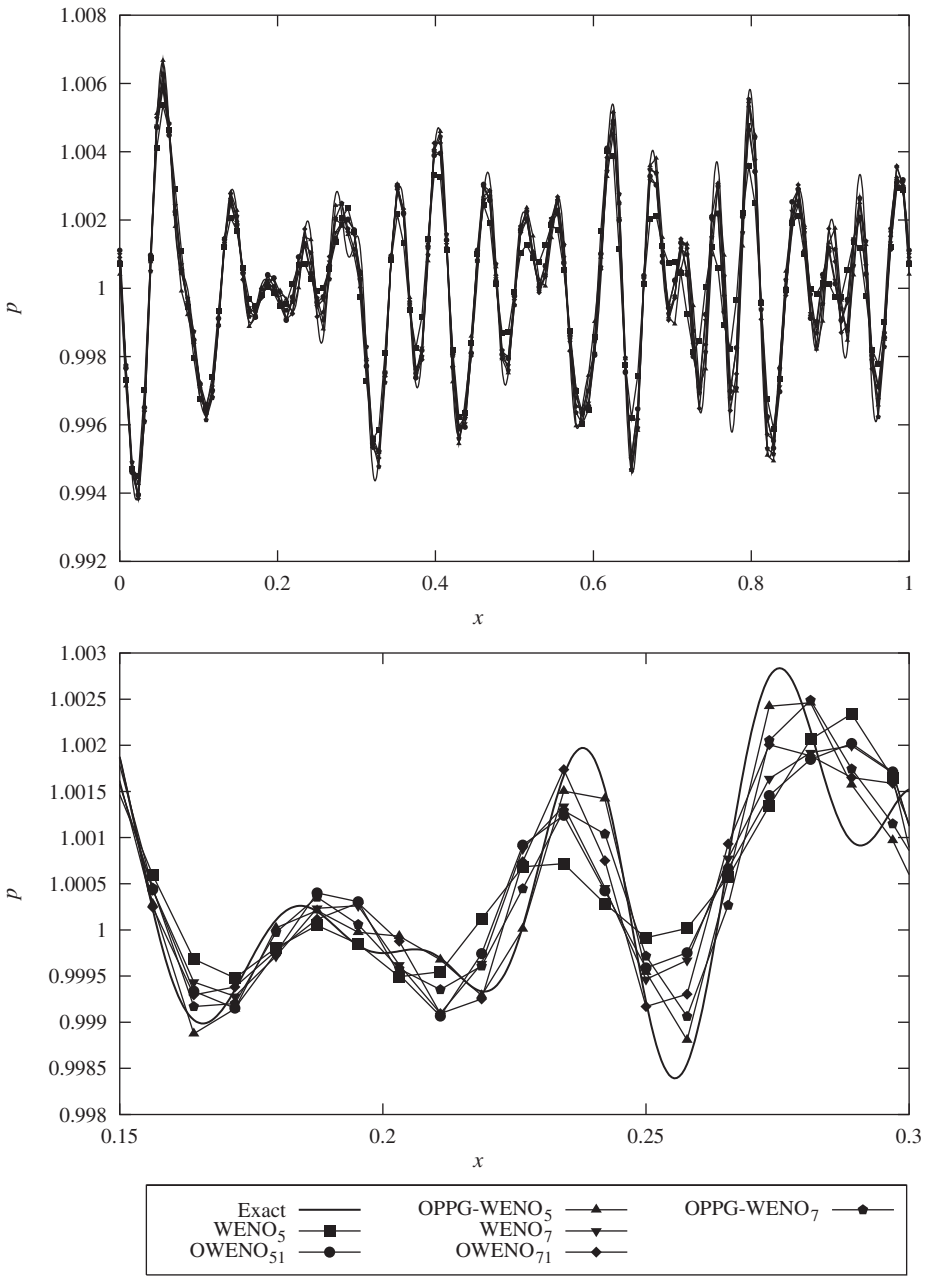

Figure 4. Broadband wave propagation. Distribution of the acoustic pressure ($k_0 = 16$, $N = 128$).

addition, the results also show that the optimization plays a major role when applied to a broadband wave whose energy content is in the high wave number range (representative of the small scales).

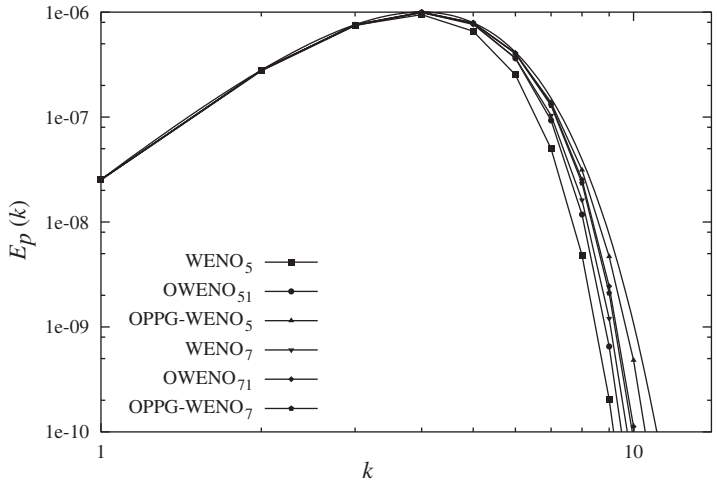

Figure 5. Broadband wave propagation. Computed pressure spectrum ($k_0 = 4,\ N = 32$).

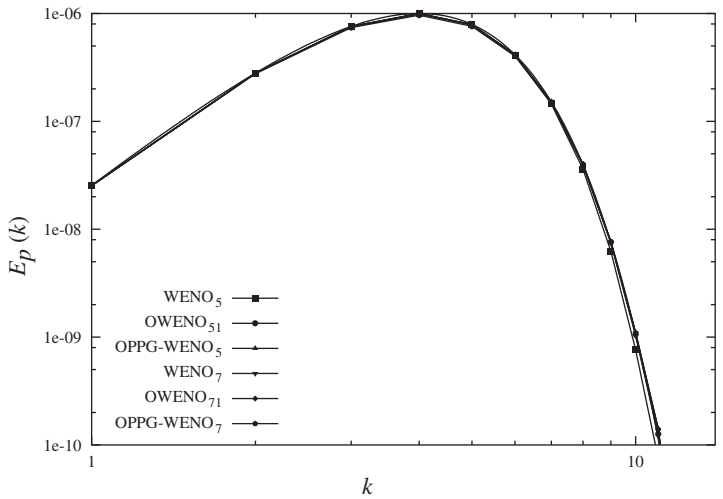

Figure 6. Broadband wave propagation. Computed pressure spectrum ($k_0 = 4,\ N = 64$).

3.2. *Shock–sound wave interaction*

This problem is characterized by the occurrence of both shocks and smooth flow features, and is appropriate to test the optimization of WENO schemes. The flow is initialized assuming a shock standing at $x = 0.5$ (with the spatial domain $0 \leqslant x \leqslant 1.$) that corresponds to a free stream Mach number $M_L = 2$ (where subscript L indicates the state ahead of the shock). Non-reflecting boundary conditions are imposed at the outflow boundary, while at the inflow

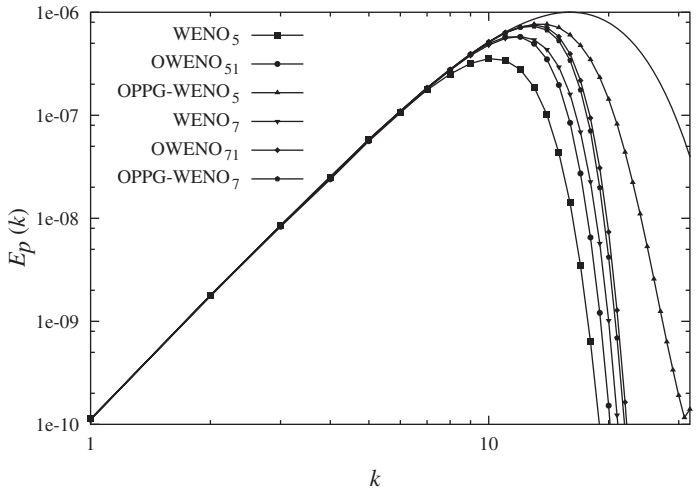

Figure 7. Broadband wave propagation. Computed pressure spectrum ($k_0 = 16,\ N = 64$).

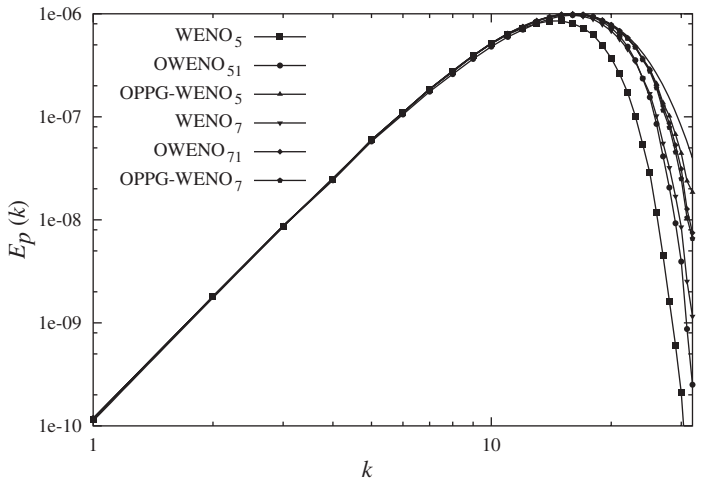

Figure 8. Broadband wave propagation. Computed pressure spectrum ($k_0 = 16,\ N = 128$).

(located at $x = 0$) we have enforced an acoustic wave with the pressure given by

$$p(0,t)/p_L = 1 + \varepsilon \sin 2\pi k\,(u_L + c_L)\,t \tag{26}$$

and the wave number per unit length (k) is set equal to 6; the density and the velocity at the left boundary are computed through isentropic assumptions.

Several computations have been carried out by varying the grid resolution. In particular, we have considered $N = 48, 64, 96, 192, 384$ that yield a wave resolution ahead of the shock $\mathrm{PPW}_L = 8, 11, 16, 32, 64$ and a wave resolution behind the shock $\mathrm{PPW}_R \approx 6, 8, 11, 21, 43$. For

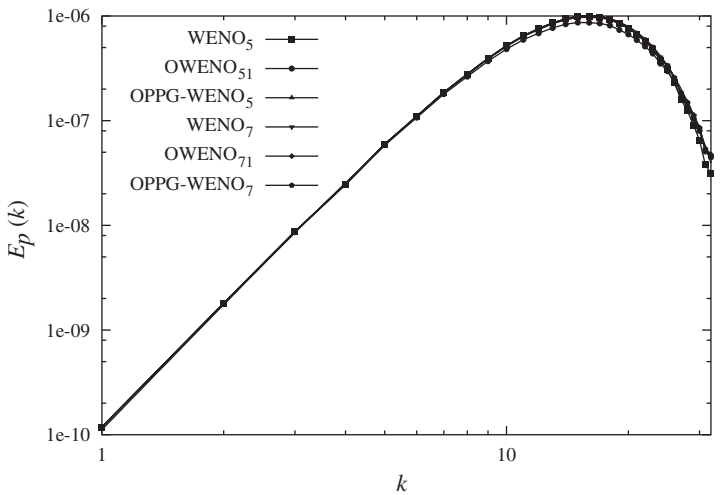

Figure 9. Broadband wave propagation. Computed pressure spectrum ($k_0 = 16,\ N = 256$).

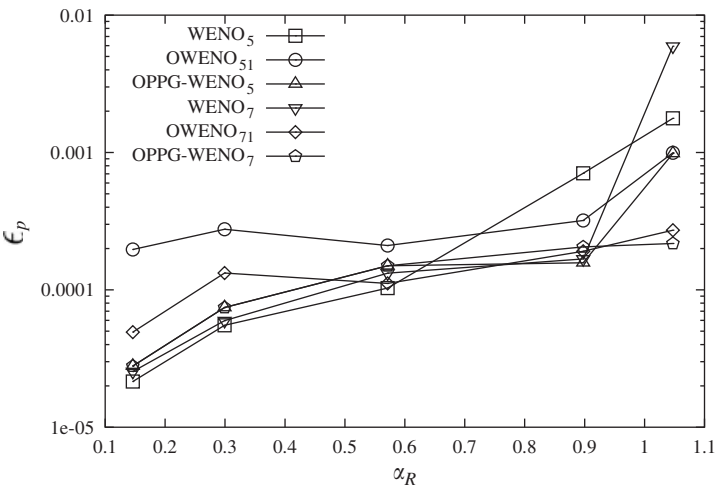

Figure 10. Shock–sound interaction. Influence of the grid resolution: distribution of computational error behind the shock as a function of the normalized wave number ($\alpha_R = 2\pi/\mathrm{PPW}_R$).

the sake of the discussion we only present the results corresponding to $N = 64$. In Figure 10 we report the distribution of the L_2 norm of the error in the pressure (ε_p) behind the shock as a function of the normalized wave number ($\alpha_R = 2\pi/\mathrm{PPW}_R$). In agreement with the findings on the dispersive and dissipative properties of the schemes (see Figure 1), the results indicate that OPPG-WENO$_5$ performs always better than OWENO$_{51}$ regardless of the points per wavelength resolution (see also Figure 11) which depicts the spatial distribution of the

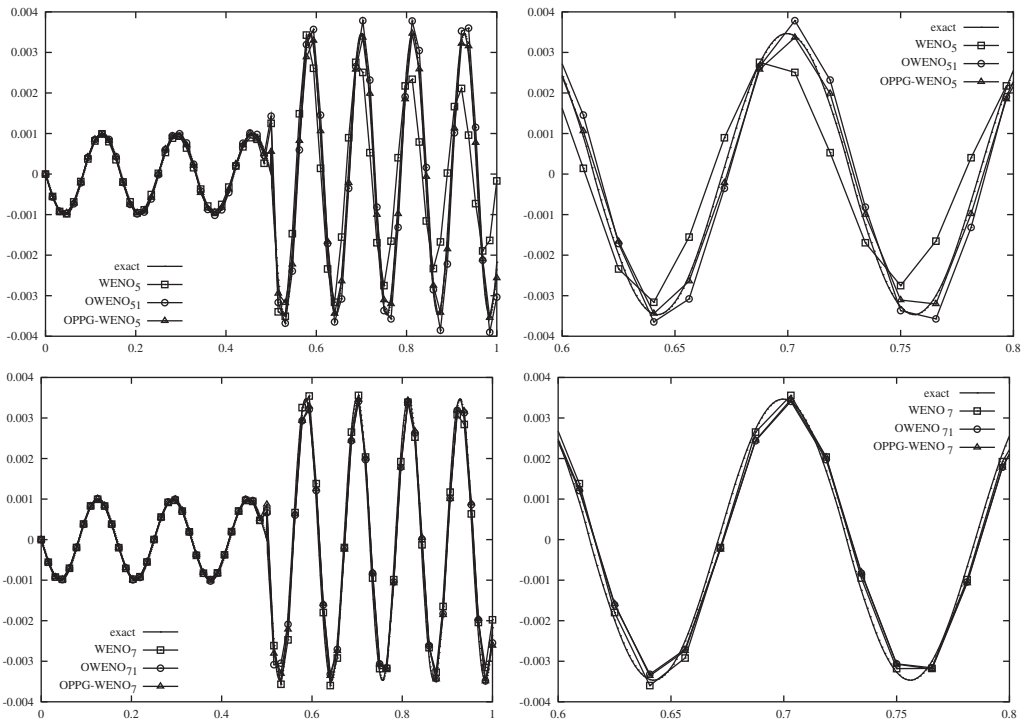

Figure 11. Shock–sound interaction. Spatial distribution of pressure disturbance ($N = 64$), $\mathrm{PPW}_L \approx 11$, $\alpha_L = 2\pi/11$; $\mathrm{PPW}_R \approx 8$, $\alpha_R \approx \pi/4$.

pressure perturbation $\delta p = p(x,t) - p(x,0)$; note that the pre-shock oscillation observed in the figure is likely due to the biasing of the stencil near a moving discontinuity as observed, but removed from their results, by Casper and Carpenter [10].

3.3. Isotropic compressible turbulence

The advantages of using an optimized scheme to increase the extent of wave number resolution have also been assessed in the context of compressible decaying isotropic turbulence. For this test case the Navier–Stokes equations have been solved, whereby the viscous fluxes have been discretized by means of a fourth order accurate compact difference approximation of Pade type [11, 12].

Let M_t, Re_t and χ be, respectively, the turbulent Mach number, the turbulent Reynolds number based on the Taylor microscale (λ) and the compressibility factor defined as

$$M_t = q/c, \quad Re_t = \overline{\rho}\, q\, \lambda/\mu, \quad \chi = \Theta/(\Omega + \Theta)$$

where q and c are, respectively, the rms of the velocity fluctuation and the mean speed of sound, while Θ and Ω are the variance of the dilatation and the enstrophy, respectively.

The selected conditions are those of the test No. 6 of Spyropoulos and Blaisdell [13], and correspond to $M_t = 0.4$, $Re_t = 2157$ and $\chi = 0.2$. The flow is initialized assuming that the initial

three-dimensional energy spectrum has the form

$$E(k) = 0.38\left(\frac{k}{k_0}\right)^4 \mathrm{e}^{-2(k/k_0)^2}$$

where the peak wave number (k_0) has been set equal to 4 as in Reference [13]. In addition as proposed by Sarkar *et al.* [14], we have assumed that the dilatational component of turbulence is in equilibrium with respect to the solenoidal part (an assumption that corresponds to the condition of acoustic equilibrium). By further assuming isentropic relations we obtain [14]

$$p'_{d_{\mathrm{rms}}} = \gamma M_{\mathrm{t}} \sqrt{\chi}, \quad \rho'_{\mathrm{rms}} = M_{\mathrm{t}} \sqrt{\chi}, \quad T'_{\mathrm{rms}} = (\gamma - 1) M_{\mathrm{t}} \sqrt{\chi}$$

where $\gamma = 1.4$ is the specific heat ratio.

In order to evaluate the optimization, several simulations have been carried out on a 64^3 grid considering the standard 5th and 7th order WENO schemes, and the OWENO and OPPG-WENO algorithms.

The most relevant quantities that need to be monitored to assess the ability of the numerical scheme to produce the correct turbulence dynamics are the enstrophy (Ω), the variance of the dilatation (Θ) and the skewness (S) where

$$\Omega = \langle (\nabla \times \underline{u}')^2 \rangle = 2 \int k^2 E_s(k)\, \mathrm{d}k$$

$$\Theta = \langle (\nabla \cdot \underline{u}')^2 \rangle = 2 \int k^2 E_{\mathrm{d}}(k)\, \mathrm{d}k$$

$$S = \frac{1}{3} \mathrm{tr}(Sk_{ij})$$

with $Sk_{ij} = \langle (\partial u_i/\partial x_j)^3 \rangle / \langle (\partial u_i/\partial x_j)^2 \rangle^{3/2}$ the skewness tensor, and E_{s} and E_{d} represent, respectively, the energy spectra associated to the solenoidal and dilatational velocity fluctuation components, respectively. Hence, in order to evaluate the different schemes, in Figure 12 we report the temporal evolutions of Ω, Θ and S obtained on the 64^3 grid, compared to an 'exact' solution, obtained on a 128^3 grid with the OPPG-WENO$_7$ scheme. As in the incompressible case (Lesieur [15]), the enstrophy exhibits a typical two-stage evolution; in particular, Ω first increases due to the vortex stretching mechanism up to a time (t_{pk}) at which it attains a peak value (Ω_{pk}), and subsequently it decreases due to viscous action. The figure shows that the values of both Ω_{pk} and t_{pk} depend upon the optimization procedure; the figure also shows that, notwithstanding the reduction of the formal order of accuracy (associated to the optimization), the increase in the wave number resolution produces an increase in the peak enstrophy values as well. Similarly, the variance of the dilatation attains a peak value that depends upon the numerical scheme. The time average values of the skewness (evaluated starting from $t = 10$, see Figure 12(c)) are reported in Table VI. and the simulations show that the OPPG-WENO$_5$ yields values close to -0.5. Recall that, for the incompressible case, the reported time-average values of the skewness vary between -0.4 [16] and -0.5 [17].

Figure 13 depicts the energy spectrum at $t = 4$ (approximately equal to twice t_{pk}) computed on the 64^3 grid (the cutoff wave number being 32); as a reference we also report the results obtained on the 128^3 grid computed with OPPG-WENO$_5$(the cutoff wave number being 64).

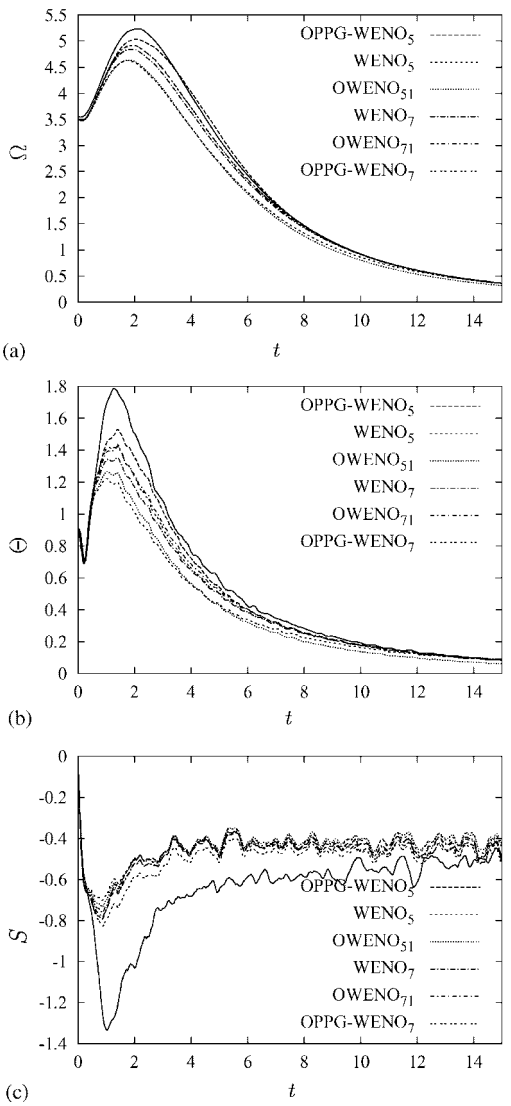

Figure 12. Isotropic compressible turbulence. Time evolution of (a), enstrophy; (b), dilatation; (c), skewness. The thick solid line represents the 'exact' solution, obtained using OPPW-WENO$_7$ on a 128^3 grid.

Note that in the figure we have indicated the value of the 'Kolmogorov' wave number determined from the fine grid results ($k_\mathrm{d} = 1/\eta \approx 32$). As observed by Porter *et al.* [18] and Garnier *et al.* [19], the dilatational energy spectrum exhibits a nearly k^{-2} decay law between 4 and 16 ($\approx k_\mathrm{d}/2$); similarly, the solenoidal energy spectrum shows a short $k^{-5/3}$ power law decay between 4 and 10. In the range $(k_0, k_\mathrm{d}/2)$, which corresponds roughly to the inertial range,

Table VI. Isotropic compressible turbulence: time average of the trace of the skewness tensor.

	OPPG-WENO$_5$	WENO$_5$,	OWENO$_{51}$	WENO$_7$	OWENO$_{71}$	OPPG-WENO$_7$
64^3	-0.45	-0.4	-0.39	-0.42	-0.43	-0.46
128^3	-0.52	—	—	—	—	—

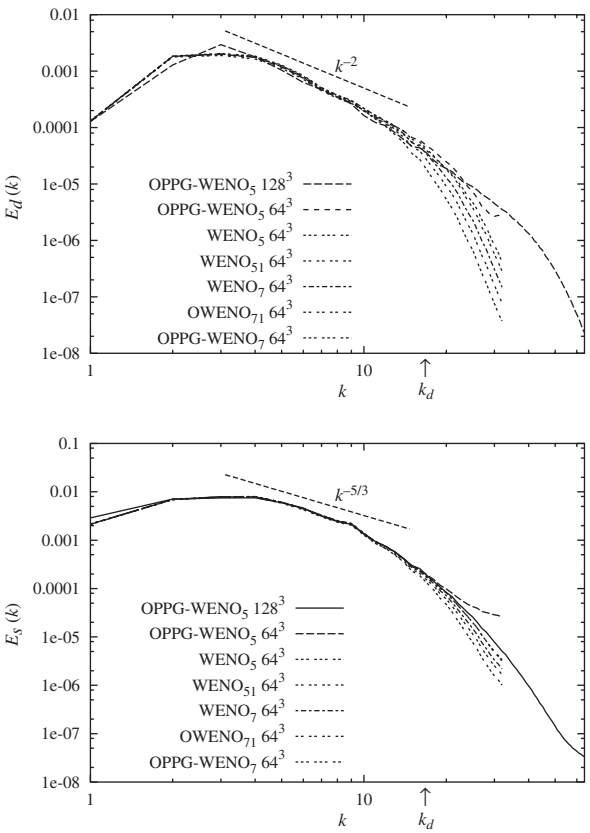

Figure 13. Compressible isotropic turbulence. Energy spectrum at $t = 4$; (a) dilatational energy contribution; (b) solenoidal energy contribution.

we have defined as a measure of the resolution, the root mean square of the energy spectrum

$$\sigma_E = \left[\sum_{k=k_0}^{k_d/2} (E(k)/E_{128}(k) - 1)^2/(k_0 - k_d/2) \right]^{1/2}$$

where E_{128} is the energy spectrum obtained with OPPG-WENO$_5$ on the 128^3 grid. The values of σ_E are reported in Table VII, which again shows that the present optimization procedure outperforms the one proposed by Wang and Chen.

Table VII. Isotropic compressible turbulence: norm of error in the inertial range (σ_E).

OPPG-WENO$_5$	WENO$_5$	OWENO$_{51}$	WENO$_7$	OWENO$_{71}$	OPPG-WENO$_7$
1.56E-2	0.16	9.7E-2	5.08E-2	4.08E-2	3.72E-2

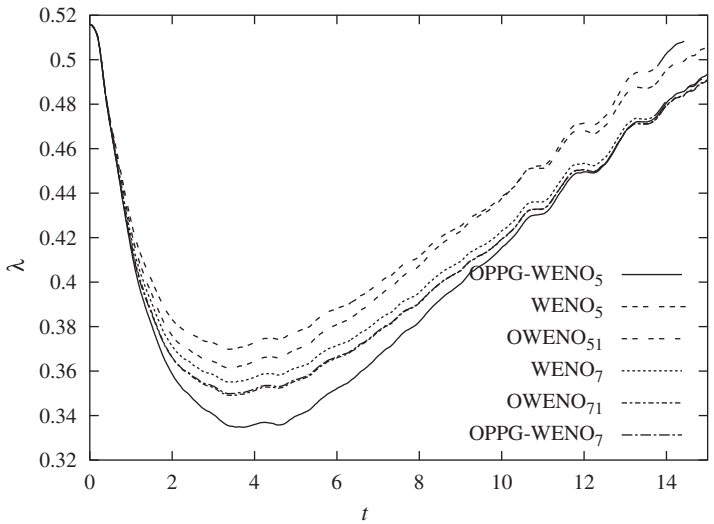

Figure 14. Isotropic compressible turbulence. Time evolution of the Taylor microscale.

For the purpose of further evaluating the properties of the optimized schemes in Figure 14 we report the distribution of the Taylor microscale as a function of time, where λ is determined through the definition

$$\lambda^2 = 15\,\frac{\nu\langle(u_i')^2\rangle}{\varepsilon_s + \varepsilon_\mathrm{d}} = 5\,\frac{\int E(k)\,\mathrm{d}k}{\Omega + 4/3\Theta}$$

where the turbulence kinetic energy dissipation has been expressed as the sum of the solenoidal (ε_s) and dilatational (ε_d) contributions (the latter being defined in terms of the variance of the dilatation as proposed by Sarkar *et al.* [14]). The figure confirms that the improvement in wave number resolution yields a smaller value of the Taylor microscale, as also observed by other authors (see Garnier *et al.* [19]).

For the purpose of comparison with the results of Spyropoulos and Blaisdell [13], we have also carried out simulations with OPPG-WENO$_7$ on a 128^3 grid (that corresponds to the same resolution of Reference [13]). In particular, in Figure 15 we report the energy spectrum at the nondimensional time $t^+ = 2.23$ (where the reference time unit is the initial eddy turnover time τ defined as the ratio of the Taylor microscale and the rms fluctuation velocity). The figure shows the good agreement of the spectra with some differences both at low and high wave numbers. With regard to the former, the discrepancies are to be ascribed to the FFT procedure adopted by Spyropoulos and Blaisdell that evaluate the energy spectra considering

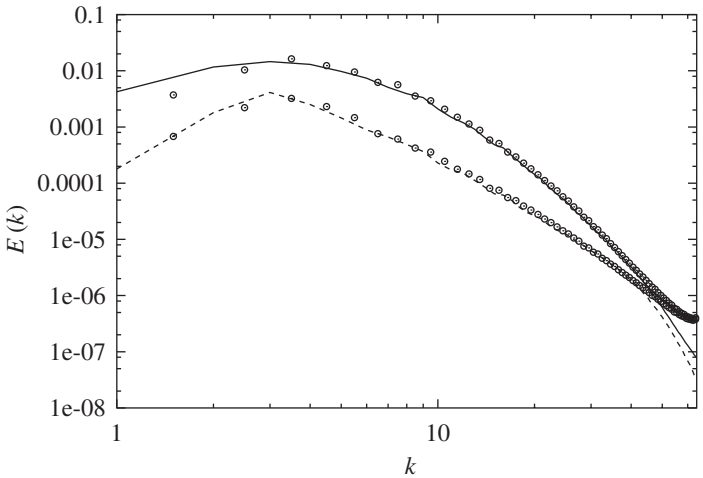

Figure 15. Isotropic compressible turbulence. Energy spectrum at $t/\tau = 2.23$ computed by OPPG-WENO$_5$ on 128^3 grid. —-, $E(k)$; – – –, $E_d(k)$; ∘, Reference [13].

non integer wave number values. With regard to the latter, we recall that Spyropoulos and Blaisdell use a pseudo-spectral Fourier collocation scheme which is less dissipative than our scheme, thus explaining the differences in the high wave number range.

4. CONCLUSIONS

In the present paper we have devised a two-level optimization strategy for WENO schemes, for multiscale compressible flows (such as compressible turbulence or aeroacoustic phenomena). The procedure combines the approaches of Weirs and Candler [3] and Wang and Chen [4]. In particular, both the interpolation coefficients of all candidate stencils and the linear weights are optimized through a minimization procedure of the numerical error. In addition, in order to minimize the error amplitude and to prevent the selection of unstable stencils, we have also considered an additional stencil so as to design a scheme with a symmetric stencil support. The optimization procedure has been evaluated both for linear and non-linear problems. With regard to the former, the Euler equations have been solved and we have considered test problems characterized either by a single scale (a sound wave propagation of a given wavelength) or by multiple scales (broadband wave propagation and shock–sound interactions). The computed results show that the proposed strategy is effective in extending the range of well resolved wave numbers. However, as the grid resolution increases, the effect of the (unavoidable) reduction of the order of accuracy of the optimized schemes dominates and the optimization is less effective. The numerical simulations also confirm that the use of a symmetric stencil support produces schemes of minimal dissipation. With regard to the non-linear test problem, the properties of the optimization have been assessed considering the direct numerical simulation of isotropic compressible turbulence. The results show that, notwithstanding the reduction of the formal order of accuracy, the increase in the wave

number resolution produces an increase in the peak enstrophy and it yields a smaller value of the Taylor microscale as also observed by other authors. Furthermore, the dilatational energy spectrum exhibits a nearly k^{-2} decay law (between 4 and 16); similarly, the solenoidal energy spectrum shows a short $k^{-5/3}$ power law decay (between 4 and 10).

ACKNOWLEDGEMENTS

The authors wish to thank Dr. G. A. Blaisdell for providing the results of compressible decaying turbulence used for comparison. The authors also thank Dr. Z. J. Wang for a fruitful exchange of information.

REFERENCES

1. Tam CKW, Webb JC. Dispersion-relation-preserving finite difference schemes for computational acoustics. *Journal of Computational Physics* 1993; **107**:262–281.
2. Lockard DP, Brentner KS, Atkins HL. High-accuracy algorithms for computational aeroacoustic. *AIAA Journal* 1995; **33**(2):246–251.
3. Weirs WG, Candler GV. Optimization of weighted ENO schemes for DNS of compressible turbulence. *AIAA paper* 1997; **97**:1940.
4. Wang ZJ, Chen RF. Optimized weighted essentially non-oscillatory schemes for computational aeroacoustic. *AIAA paper* 2001; **1101**.
5. Osher S, Chakravarthy S. Upwind schemes and boundary conditions with applications to Euler equations in general coordinates. *Journal of Computational Physics* 1983; **50**:447.
6. Liu XD, Osher S, Chan T. Weighted essentially non-oscillatory schemes. *Journal of Computational Physics* 1994; **115**:200.
7. Jiang GS, Shu CW. Efficient implementation of weighted ENO schemes. *Journal of Computational Physics* 1996; **126**:202.
8. Shu C-W. Essentially non-oscillatory and weighted essentially non-oscillatory schemes for hyperbolic conservation laws. In *Advanced Numerical Approximation of Non-linear Hyperbolic Equations*, Cockburn B, Johnson C, Shu C-W, Tadmor E, Quarteroni A (eds). Lecture Notes in Mathematics, vol. 1697. Springer: Berlin, 1998; 425–432.
9. Balsara D, Shu C-W. Monotonicity preserving weighted essentially non-oscillatory schemes with increasingly high order of accuracy. *Journal of Computational Physics* 2000; **160**:405.
10. Casper J, Carpenter MH. Computational Considerations for the Simulation of Shock-induced Sound, NASA TM 110222, 1995.
11. Lele SK. Compact finite difference schemes with spectral-like resolution. *Journal of Computational Physics* 1992; **103**:16.
12. Grasso F, Pirozzoli S. Asymptotic scaling of a decaying turbulent compressible vortex. *Physics of Fluids* 1999; **11**:1636.
13. Spyropoulos ET, Blaisdell GA. Evaluation of the dynamic model for simulations of compressible decaying isotropic turbulence. *AIAA Journal* 1996; **34**:5.
14. Sarkar S, Erlebacher G, Hussaini MY, Kreiss HO. The analysis and modelling of dilatational terms in compressible turbulence. *ICASE Report* 1989; 89–79.
15. Lesieur M. *Turbulence in Fluids*. Kluwer Academic: Dordrecht, 1990.
16. Batchelor GK. *Townsend Proc. R. Soc. London* 1949; **199**:238.
17. Vincent A, Meneguzzi M. The spatial structure and statistical properties of homogeneous turbulence. *Journal of Fluid Mechanics* 1991; **225**:1.
18. Porter DH, Poquet A, Woodward PR. Kolmogorov-like spectra in decaying three-dimensional supersonic flows. *Physics of Fluids* 1994; **6**(6):2133.
19. Garnier E, Mossi M, Sagaut P, Comte P, Deville M. On the use of shock-capturing schemes for large-eddy simulation. *Journal of Computational Physics* 1999; **153**:273–311.
20. Erlebacher G, Hussaini MY, Kreiss HO, Sarkar S. The Analysis and Simulation of Compressible Turbulence. *Theoretical Computational Fluid Dynamics* 1990; **2**:73–95.
21. Grasso F, Meola C. Euler and Navier–Stokes equations for compressible flows: finite volume methods. In *Handbook of Computational Fluid Mechanics*, Peyret R (ed.). Academic Press: New York, 1996; 159.
22. Grasso F, Pirozzoli S. Shock Wave–Vortex Interactions: Shock And Vortex Deformations, And Sound Production. *Theoretical Computational Fluid Dynamics* 2000; **13**:421.

23. Grasso F, Pirozzoli S. Simulations and analysis of the coupling process of compressible vortex pairs: free evolution and shock induced coupling. *Physics of Fluids* 2001; **13**:1343.
24. Poinsot TJ, Lele SK. Boundary conditions for direct simulations of compressible viscous reacting flows. *Journal of Computational Physics* 1992; **101**:104.
25. Shu CW, Osher S. Efficient implementation of essentially non-oscillatory shock-capturing schemes. *Journal of Computational Physics* 1988; **77**:439.
26. Thompson KW. Time-dependent boundary conditions for hyperbolic systems. *Journal of Computational Physics* 1987; **68**:1–24.
27. Thompson KW. Time-dependent boundary conditions for hyperbolic systems, II. *Journal of Computational Physics* 1990; **89**:439–461.

